4.2 Technological Laboratories and Instrumental Developments

4.2.1 Technological Laboratory LMU

H.J. Maier, R. Grossmann, H.U. Friebel, and D. Frischke

Target preparation by high vacuum sputter deposition

This important technology has been further improved. A schematic drawing of our new experimental set-up is shown in Fig. 1 A saddlefield ion source of the B11W type, supplied by Atom Tech Ltd., West Moseley, England, is utilized to generate a 10 keV Xe^+ ion beam of 0.1 mA current intensity. The beam is directed to impinge, at an angle of 30^o to that of horizontal, upon the isotopically enriched coating material. This is normally made into the shape of a 0.3 - 1 mm thick tablet of 7 mm diameter and placed on a graphite support at a distance of 30 mm from the source. As described in detail in [1], the source is fitted to a manipulator, which allows to adjust the beam spot to the coating material by visual inspection during operation. In order to achieve a good collection efficiency, the substrate is mounted at a short distance of 20 mm above the beam spot. Immoderate thickness variation across the deposited film due to this close geometry is avoided by rotating the substrate at a tilt of 30^o-60^o with respect to the normal line of the tablet. Tilting of the substrate results in a decrease of its solid angle, as seen from the beam spot, and, as a consequence, produces a more homogeneous film thickness distribution. Typically, the relative thickness variation across a target of 10 - 15 mm diameter can be reduced to about 5 % by this precaution.

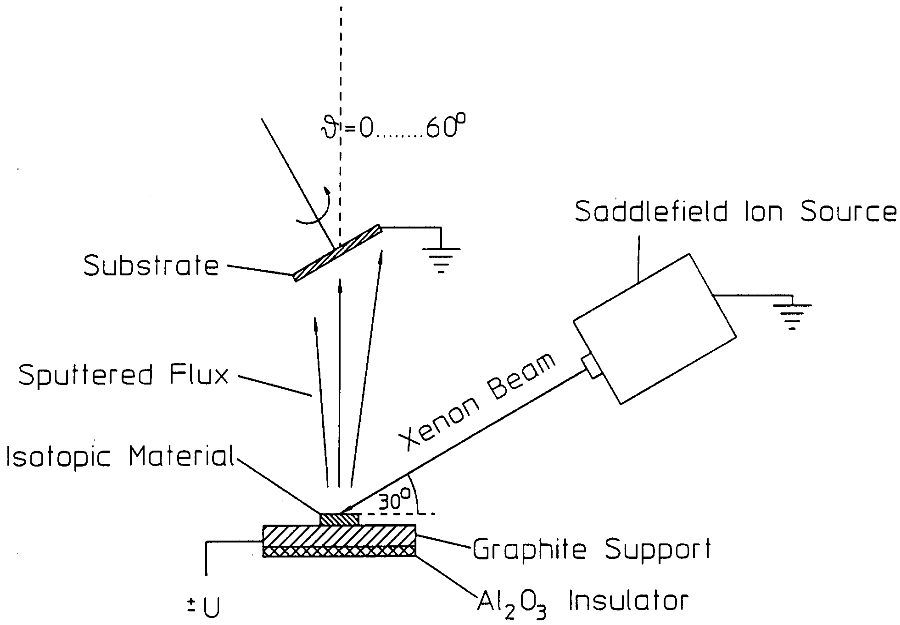

Fig. 1: Schematic experimental setup

In order to suppress the secondary electrons emerging from the coating material, a bias is applied between the graphite support and the substrate. Electron bombardment during deposition may cause damage like internal stress in a growing thin film.

A cryopump having a pumping speed of $5000\,\mathrm{ls}^{-1}$ for N_2 and $12000\,\mathrm{ls}^{-1}$ for H_2O allows the evacuation of the deposition chamber to an ultimate pressure of less than $5{\cdot}10^{-8}$ mbar. The corresponding residual gas spectrum is shown in Fig. 2 demonstrating the absence of hydrocarbons. During operation, Xe gas of 99.998 % purity is supplied to the saddlefield source at a flow rate of 0.01 scc/min. Due to the high pumping speed of the cryopump, the Xe-partial pressure in the chamber stays as low as 10^{-7} mbar.

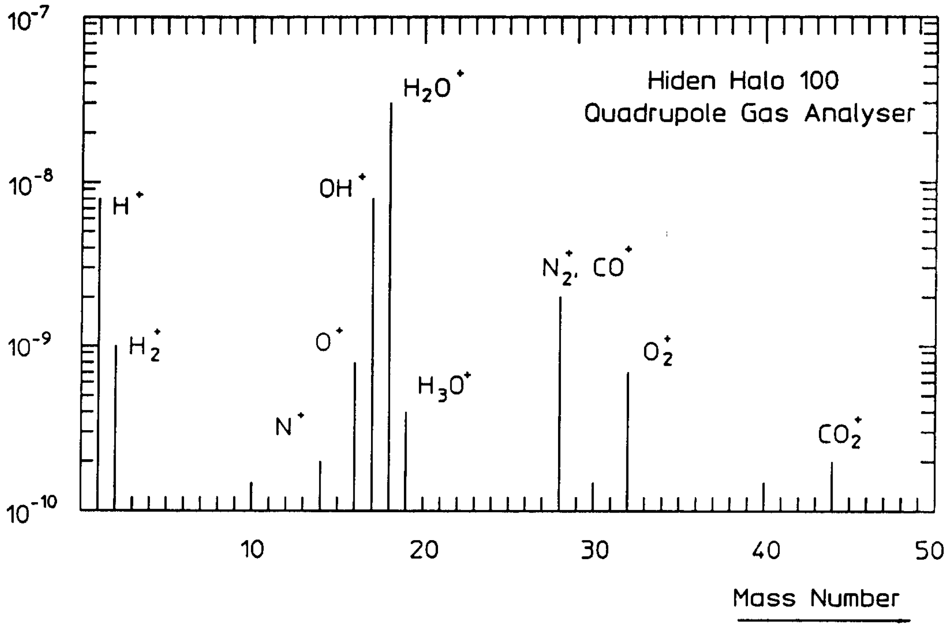

Fig. 2: Residual gas spectrum in the deposition chamber after pumpdown to $5{\cdot}10^{-8}$ mbar

An average of 1.5 mg of isotopic source material was found to be sufficient to prepare a target of $100\,\mu\mathrm{g\,cm}^{-2}$ thickness, nearly independent of the specific element. More than 300 samples have been made so far, including self supporting metallic targets of Cr, Mo, Ru, Hf, W, Os, Pt, and Th of a few hundred $\mu\mathrm{g\,cm}^{-2}$ thickness. All these targets are sturdy, pinhole-free, and virtually free from strain. They were prepared with excellent reproducibility and negligible waste, using a mixture of betaine monohydrate and sucrose as a parting agent. ^{186}W foils of 350-550 $\mu\mathrm{g\,cm}^{-2}$ thickness and 15 mm diameter, taken from the batch production, were of sufficient strength to be successfully stretched to form very flat targets for use in recoil - distance measurements of nuclear lifetimes [2].

Most of the metal targets were prepared within 2 - 5 hours at deposition rates between 50 and $150\,\mu\mathrm{g\ cm}^{-2}\mathrm{h}^{-1}$. More time is required for the reactive sputter deposition of oxide and nitride films. The average deposition rate for these film types is 30 - $40\,\mu\mathrm{g\,cm}^{-2}\,\mathrm{h}^{-1}$.

Target films in oxide form require thin carbon backings without exception. Metal oxide films can be of interest aiming towards isotopically enriched oxygen targets or targets of enriched metal isotopes in form of their oxides. So far, only targets of the latter category have been prepared as for instance $^{92,96}ZrO_2$ and ^{87}SrO. In these cases, the pelletized oxide powder serves as coating material, which is bombarded by the Xe^+ ion beam. According to our experience, crystalline oxide powders are partially degraded by particle bombardment. Therefore, at the standard partial pressure of 10^{-9} mbar for O_2 in our deposition chamber, the resulting films are suboxides of grey, indefinite appearance. If, however, the deposition is performed at an O_2-partial pressure of 10^{-7} mbar, films with distinctive interference colours are formed. They consist of stoichiometric oxides, as confirmed by standard RBS analyses [3]. The required O_2-partial pressure is obtained by feeding $^{nat}O_2$ gas of 99.99 % purity into the deposition chamber, using a precision stainless steel needle valve. Suppression of secondary electrons originating from the coating material by application of a bias of 200 V and maintaining a deposition rate of 30 - 35 μg cm^{-2} h^{-1} results in films with minimum internal stress. By this procedure, stoichiometric oxide films in the thickness range between 50 and 400 μg cm^{-2} have been prepared.

Reactive sputtering also provides access to nitrogen targets in form of metal nitrides. As a case study for the feasibility of ^{15}N targets, ^{nat}Ti was sputtered at an N_2-partial pressure of 10^{-6} mbar, which was achieved by feeding 10 scc h^{-1} of $^{nat}N_2$ gas of 99.99 % purity into the deposition chamber. Using a 25 μg cm^{-2} thick carbon foil as substrate, a yellowish film condensed at a rate of 40 μg cm^{-2} h^{-1}, containing Ti, N, and O in the atomic ratio of 1, 0.72, and 0.15, respectively, as determined by ERDA analytical techniques [4]. Due to its high nitrogen content, likely in form of TiN, a film made by this procedure would serve as a suitable nitrogen target. However, its high oxygen contamination is most unsatisfactory. It can be explained by occlusion of H_2O molecules from the residual gas in the growing film either by physisorption or by chemisorption [1]. Improvement of the basic vacuum in the sputtering chamber by one order of magnitude should enable the preparation of virtually oxygen-free TiN targets. Appropriate efforts are in progress.

Prepariation of self supporting, metallic Hf targets from isotopically enriched HfO_2

For preliminary studies in connection with projected Coulomb excitation experiments starting from the K = 16+ isomer in ^{178}Hf, self-supporting, metallic targets of the stable isotopes ^{176}Hf, ^{177}Hf, ^{178}Hf, ^{179}Hf and ^{180}Hf had to be provided. For this purpose, a practicable method had to be found to convert HfO_2, the standard form of delivery of enriched Hf isotopes, into Hf metal of sufficient purity to allow further processing into thin foils. Since Hf shows a high tendency to dissolve its own oxide, metallothermic reduction of HfO_2 with Ca or Mg is expected to result in brittle Hf metal containing appreciable amounts of oxygen. Removal of the oxide requires the application of complex metallurgical procedures, which do not work satisfactorily with small quantities of isotopic material. On the other hand, the preparation of Hf from a fluorine compound like HfF_4 seems to be more promising, since traces of fluorides can be easily removed via conventional refining techniques, e.g., high vacuum electron beam melting.

Following this general line, the targets were prepared in a three-step process:

A. Conversion of HfO_2 into HfF_4 by the NH_4 HF fusion method

A mixture of HfO_2 with a 30% excess of high-purity NH_4F HF is placed in a Pt tray and brought to reaction in a tube-shaped Inconel working chamber at 800 K:

$$HfO_2 + 4NH_4F \cdot HF \xrightarrow[1000 mbar Ar]{800K} HfF_4 + 4NH_4F + 2H_2O.$$

Heating is performed by means of an electrical resistance furnace. Dry Ar gas is used to purge the chamber at a rate of 1 l min^{-1} to remove the volatile reaction by-products NH_4F and H_2O and excess $NH_4F \cdot HF$ from the system. The reaction is allowed to come to completion within about 12 hours. The yield is better than 99%.

The resulting HfF_4 is of excellent purity. An x-ray structure analysis based on the JCPDS powder diffraction file [5] does not show evidence for the presence of oxyfluorides within the detection limits of 1%. The absence of oxygen at this stage of the procedure is a major condition for the successful preparation of Hf metal target foils.

B. Hf metal preparation

Bomb reduction techniques are applied to obtain metallic Hf from HfF_4. A stainless steel bomb holding a tantalum liner is stuffed with a mixture of HfF_4 plus twice the stoichiometric amount of vacuum distilled Na as reducing agent, and sealed with a Swagelok cap. This is accomplished in a glovebox containing a dry argon atmosphere. The sealed bomb is heated in a high vacuum furnace to a temperature of 1400 K for a period of 3 hours. The formation of Hf metal takes place in Ar according to the reaction equation

$$HfF_4 + 4Na \xrightarrow[Ar]{1400K} Hf + 4NaF.$$

After opening the bomb in ambient air, absolute ethanol is first added to the reaction mixture to extract the excess Na. Separation of the NaF reaction by-product is accomplished by treatment with hot soda lye, boiling in 6N HCl and finally rinsing with deionized water. As a result, Hf is obtained in form of a fine-grained metal powder of grey appearance, which is submitted to electron beam melting for final purification. The reaction yield is approximately 75% for 100 mg samples and 90% for 300 mg samples.

C. Target preparation by ion beam sputter deposition techniques

Self supporting metallic targets of ^{nat}Hf and the isotopes ^{176}Hf, ^{177}Hf, ^{178}Hf, ^{179}Hf, and ^{180}Hf in the thickness range between 100 and 300 $\mu g\,cm^{-2}$ have been prepared by ion beam sputter deposition techniques. The Hf films were condensed at room temperature on glass substrates coated with a parting agent, subsequently floated in deionized water, and finally lifted onto stainless steel frames with a 13 mm diameter hole. A mixture of betaine monohydrate and saccharose forms a suitable parting agent resulting in pinhole-free target foils of excellent mechanical performance. A more detailed description of the whole procedure is given in [6].

[1] H.J. Maier, Nucl. Instr. and Meth. A303 (1991) 172
[2] H. Hübel, Institut für Strahlen- u. Kernphysik, Universität Bonn, Germany, private communication
[3] W. Lang, Institut für Festkörpertechnologie der Fraunhofer-Gesellschaft München, Germany, private communication
[4] W. Assmann, LMU, private communication
[5] JCPDS - Powder Diffraction File, compiled by the Joint Committee on Powder Diffraction Standards, 1601 Park Lane, Swarthmore, Pennsylvania 19081, USA
[6] H.J. Maier, H.U. Friebel, D. Frischke and R. Grossmann, Proc. 16th INTDS World Conference, to be published in Nucl. Instr. and Meth. A

4.2.2 Target Laboratory TUM

P. Maier-Komor, G. Dollinger, Ch.M. Frey, Maria Katharina Nacke, and Anna Stolarz [a]
[a] Heavy Ion Laboratory of Warsaw University, Poland

Status of the system for laser plasma ablation deposition of carbon
(Carbon stripper foils) (in cooperation with H.-J. Körner)

In the Jahresbericht 1991 was reported about the problems with the pulsed Nd:YAG laser, which even caused a damage of the laser rod. The reasons for the failures were not found until the laser was lifted only on one side during transportation. After this there was despite of maximum laser pumping power no laser output. Now it was easy to detect the error. One of the 90°; deflection mirrors between oscillator and amplifier could not be fixed in his housing due to too large fabrication tolerances. The laser system had to be completely realigned and delivers now nearly the specified laser power, unfortunately the maximum laser power density cannot be achieved due to an unexplained pulse length of 12 ns instead of the specified 10 ns. The laser company promised to solve this problem in the near future. For the preparation of lpa-foils (carbon stripper **foils** prepared by **l**aser **p**lasma **a**blation deposition) the 20% longer pulse width is of no meaning because as explained later these carbon films will be prepared with only 2 GW/cm^2 laser power density.

Fig. 1 shows schematically the ultrahigh vacuum box coater. It has a cubic shape with 50 cm inner edge length. It is completely metal sealed with two exceptions: the entrance window for the laser beam and the main glass door are viton sealed. On the outside of the 20 mm thick glass door a 20 cm $\times$ 20 cm protection window against the laser light is mounted in an aluminium frame, which covers completely the outside of the glass door. The laser and all the optical components are mounted in light tight housings. In this way the laser processing can be observed without wearing laser protection goggles.

The laser entrance window for the laser light into the box coater is an optical plane 10 cm Ø and 1 cm high crown glass commercially coated with an antireflection multilayer on the atmospheric side and coated with a $\lambda/4$ layer of cryolite (Na_3AlF_6) on the vacuum side. The transmission of the laser light (λ = 1064 nm) through this window is $\approx$ 98%. This cryolite coating can be etched away together with the carbon deposit, which is necessary after every third charge due to the increasing absorption of the growing carbon film. The recoating of the window with cryolite is done in one of our standard evaporation plants.

In the meantime a problem was faced with the antireflection layer cryolite on the vacuum side of the intrance window. It did not stand the high power density a thicker layer of $3\lambda/4$ instead of the $\lambda/4$ helped but did not solve completely the problem. That is why it is planned to reduce the power density at the intrance window by installing an upcollimator of 7.5 : 1, which is nearly the optimum one in combination with a focusing lens of a focal length of 100 cm when focusing with spherical lenses. Consequently the focusing lens must be exchanged by a bigger one (80 mm Ø) and a new dielectric mirror (100 mm Ø) for wobbling the laser beam will be installed.

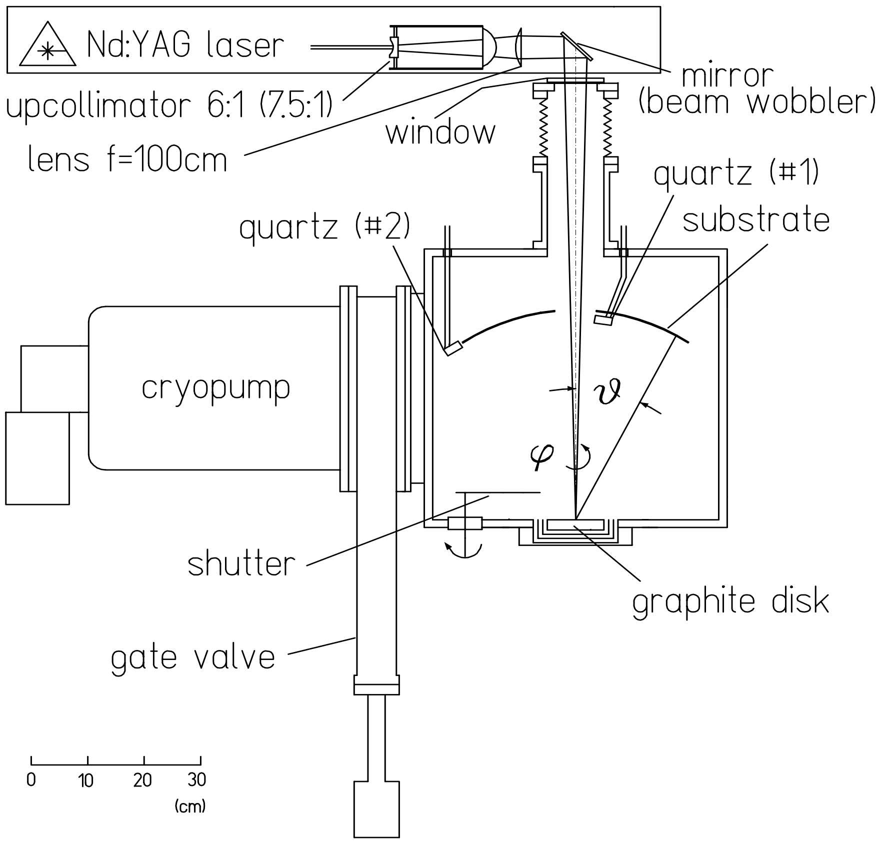

Fig. 1: Schematic drawing of the ultrahigh vacuum apparatus for laser plasma ablation-deposition of carbon.

Three quartz crystal sensors were installed from the top of the box coater for measuring the spatial distribution of the deposit from the carbon plasma. One quartz crystal sensor (#1) was mounted as close as possible to the laser beam at a polar angle $\vartheta = 6°$, an azimuth angle $\varphi = 0°$ and at a distance of 40 cm from the center of the graphite disk surface. This sensor was fixed for all experiments and used for normalization. The other two quartz crystal sensors were used for measuring the angle distributions of the carbon deposition rates. Both were mounted at the same polar angle ϑ but by $\pi/2$ differing azimuth angles φ. Sensor #2 was mounted at $\varphi = \pi$ and sensor #3 at $\varphi = \pi/2$. The distance of these two quartz crystal sensors from the target center was 30 cm for all measurements. All three quartz crystal sensors were mounted with the median perpendicular of their sensitive area adjusted to the target center. Due to the spirally scanning of the focused laser beam on the graphite disk the total deposition is always a mean value from an angle range $\Delta\vartheta = 17°$.

The tuning of the laser power density on the surface of the graphite target cannot be performed by changing the pumping power of the arc lamps. The high peak pulse power of $\approx$ 40 MW in connection with the high repetition rate of 50 Hz require a careful adjustment of the whole laser system which takes into account the temperature dependent lens formation of the YAG rods. This setting was done for full power of the laser system with the highest repetition rate of 50 Hz.

That is why the desired laser power density on the graphite target was obtained by changing the beam spot size on the target by means of the distance between the focusing lens (f = 100 cm) and the target. The reduced power density was set by a larger distance than the focal length between convex-plano lens and target. The power density was then calculated according the applicability of geometric optics.

Carbon deposition rates were measured as a function of laser power density on the graphite target. The quartz crystal sensor #1 was used for normalization of the data from the other two sensors. The substrate dome will be designed for a source to substrate distance of 38 cm. For this distance all measured deposition rates are normalized and compiled in table 1 for a power density range of 0.5 to 230 GW/cm^2. For better comparison the deposition rates are normalized on the area of the respective beam spot. These area related rates are constant within the given error for the energy range of 0.5 to 10 GW/cm^2. Only the highest power density results in a higher area related rate which is of no significance for the planned deposition process, because the deposition rate depends linearly on the beam spot area. That is why it is suggested to prepare the lpa-films at the lowest possible power density at which the plasma conditions are still sufficient for the desired film structure.

Power density [GW/cm^2]	Measured depositon rate [μg cm^{-2} min^{-1}]	Deposition rate per beam spot area [μg cm^{-4} min^{-1}]
0.5	2.6 ± 0.5	43 ± 9
0.6	1.5 ± 0.3	29 ± 6
0.7	1.9 ± 0.4	42 ± 8
1.0	1.2 ± 0.2	40 ± 8
1.4	0.72 ± 0.14	33 ± 7
2.0	0.49 ± 0.10	36 ± 7
3.7	0.26 ± 0.05	34 ± 7
9.4	0.13 ± 0.03	38 ± 8
230	0.07 ± 0.01	350 ± 130

Table 1: Deposition rates in dependence of the laser power density on the graphite target

Deposition rates in dependence from the polar angle ϑ were investigated at three different laser power densities: 230 GW/cm^2, 1.6 GW/cm^2 and 0.7 GW/cm^2. These rates measured with the two quartz crystal sensors for the different polar angles ϑ were normalized by the respective rates measured with the sensor at $\vartheta = 6°$. The data are plotted in fig. 2. For 230 GW/cm^2 (fig. 2a) and 1.6 GW/cm^2 (fig. 2b) the deposition rates can be fitted by an angle distribution of $\cos^{1.5}(\vartheta)$. For the low power density of 0.7 GW/cm^2 (fig. 2c) the angle distribution cannot be fitted by a unique power of the cosine function, for angles $\vartheta \geq 40°$ a $\cos^2(\vartheta)$ distribution can be approximated, for smaller angles, however, a steep rise was observed.

With the setup of the quartz crystal sensor #2 ($\vartheta = \vartheta$; $\varphi = \pi$) and the sensor #3 ($\vartheta = \vartheta$; $\varphi = \pi/2$) all data as a function of laser power density could be investigated on their isotropy of the azimuth angle φ. Fig. 4 shows the different deposition rates for the two azimuth angles φ at a power density of 1.6 GW/cm^2, which is in the range where the carbon stripper foils should be prepared as will be proved later on.

The reason for this anisotropy with φ is the shape of the laser beam spot on the graphite target which is elliptic due to the mode pattern of the laser system. This unisotropy of the deposition rate due to the elliptic shape of the beam spot can be explained qualitatively. The short axis of the ellipse may represent a point source with isotropic carbon propagation whereas the long axis stands more for an area source, which means that the quartz crystal sensor in direction of the long axis detects a lower rate.

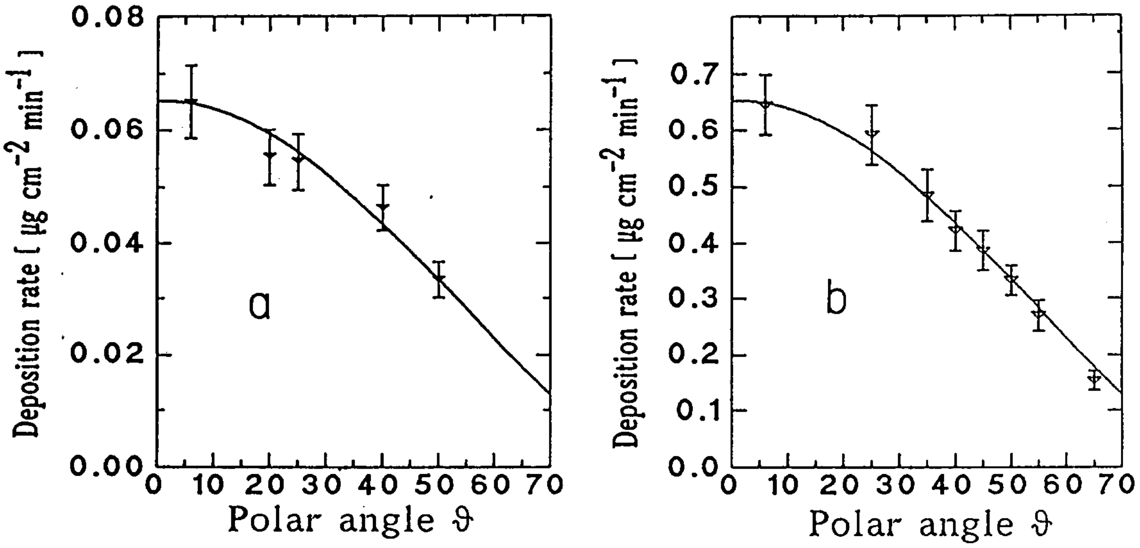

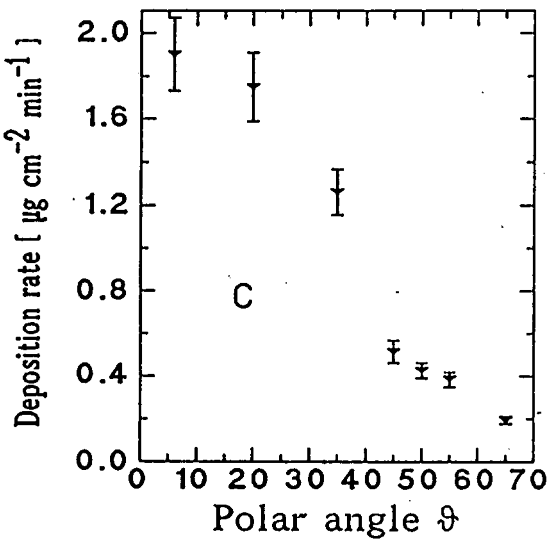

Fig. 3: Carbon deposition rate as a function of the polar angle ϑ.
a) for a power density of 230 GW/cm^2
b) for a power density of 1.6 GW/cm^2
c) for a power density of 0.7 GW/cm^2

The crystalline orientation of the nanocrystals in the selfsupporting carbon foil was measured at eleven various power densities from 0.4 to 230 GW/cm^2 at a polar angle $\varphi = 25°$. This was done by the analysis of the densitometer plots from transmission electron diffraction rings of the heat treated carbon foils. For an isotropic orientation the ratio is $I_{002}/I_{10} = 2.6$, if all (002)-planes are oriented parallel to the foil surface then the ratio is $I_{002}/I_{10} = 0$. Both values are indicated on the data plot of fig. 4. For power densities below 0.5 GW/cm^2 all hexagonal planes are oriented parallel to the surface like in carbon foils prepared by thermal evaporation-condensation technique. In the range of 0.5 to 0.7 GW/cm^2 the texture of the foil decreases continuously. For power densities greater than 0.7 GW/cm^2 all ratios I_{002}/I_{10} indicate the desired isotropic orientation of the nanocrystals.

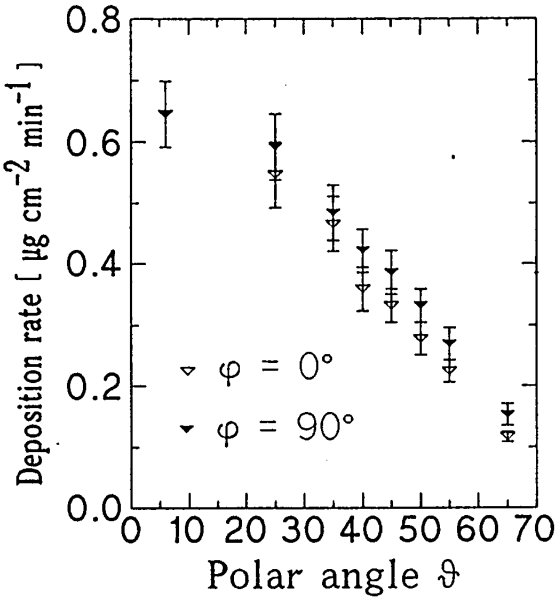

Fig. 4: Deposition rates measured for a power density of 1.6 GW/cm^2 as a function of polar angle ϑ for two azimuth angles φ.

The crystalline orientation of the nanocrystals in the selfsupporting carbon foil was measured in dependence of the deposition at a polar angle ϑ. These data were taken for power densities of 1.6 GW/cm^2 (fig. 6a) and 0.7 GW/cm^2 (fig. 6b), where the last one is the measured minimum power density for which isotropic orientation was found at $\vartheta = 25°$.

For 1.6 GW/cm^2 the isotropic orientation is found up to a polar angle $\vartheta = 45°$. For $\vartheta > 45°$ a structure changing takes place which results already at $\vartheta = 55°$ in the unisotropic structure as known for thermal evaporation-condensation of carbon. This transition is in reality much sharper than indicated in fig. 6a due to the gyration of the point source, which implies a polar angle range $\Delta\vartheta = 17°$.

For the power density of 0.7 GW/cm^2 the crystalline isotropy disapears already at much smaller polar angles. Even at $\vartheta = 35°$ the ratio of $I_{002}/I_{10} = 1.9 \pm 0.6$ shows unambiguously a deviation from the isotropy. For $\vartheta \geq 45°$ the carbon layer exhibits the crystalline orientation known from thermal evaporation.

Consequences for the setup for preparing lpa-carbon stripper foils are as follows:

For economical reasons and to minimize the influence of the residual gas the carbon ablation should be performed with a maximum deposition rate. The highest deposition rate was observed at the lowest laser power density, which was adjusted with the biggest beam spot area on the target. The minimum power density necessary to obtain isotropic orientation was 0.7 GW/cm^2 (fig. 5), but it could be applied only for polar angles $\vartheta < 25°$ (fig. 6b). As a compromise the lpa-carbon stripper foils will be prepared at a power density of 2 GW/cm ^{2} with a substrate mount of an outer diameter up to a polar angle $\vartheta \geq 35°$. A unforeseen power drop of 20 % (fig. 6a) would be still tolerable with these parameters. Nevertheless the laser power will be measured in the vented vacuum chamber before each deposition charge.

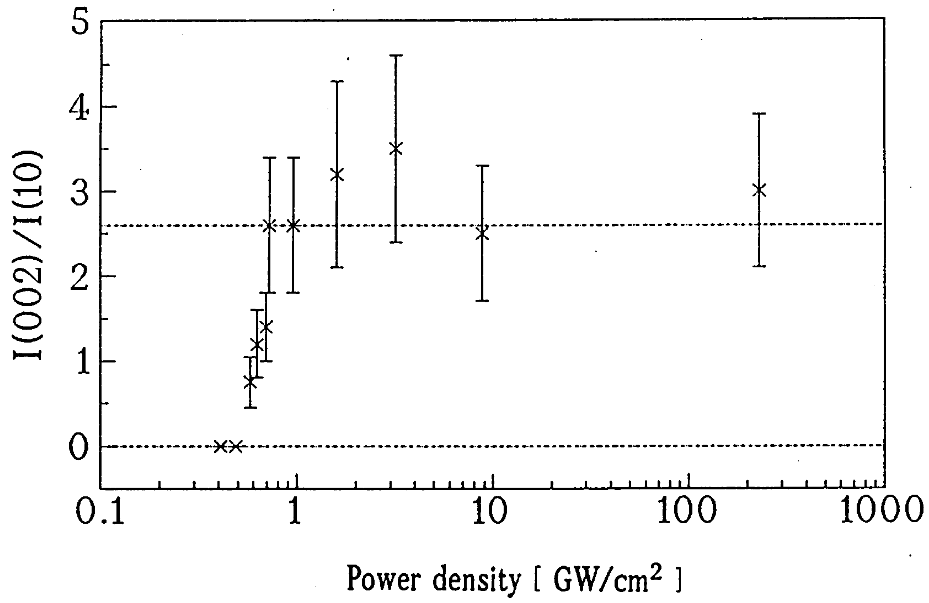

Fig. 5: Crystalline orientation as a function of laser power density on the target.
$I_{002}/I_{10} = 0$ means all hexagonal planes are parallel to the surface
$I_{002}/I_{10} = 2.6$ means isotropic orientation of the nanocrystals

It was demonstrated that the deposition rate in dependence of the polar angle ϑ follows a $\cos^{1.5}(\vartheta)$-distribution. In order to compensate the dependence of the distribution for a constant deposition rate the distance $R(\vartheta)$ of the substrate from the target surface center must be normalized by the square root of the ϑ-dependence:

$$R(\vartheta) = R_0 cos^{0.75}(\vartheta)$$

where R_0 is the distance from the target surface center at a polar angle $\vartheta = 0°$. A substrate dome with $R_0 = 40$ cm is under construction. As demonstrated by fig. 4 there is some thickness variation with the azimuth angle φ which requires a rotation of the substrate dome during deposition. The drive of the dome rotation will be done with a ultrahigh vacuum stepping motor.

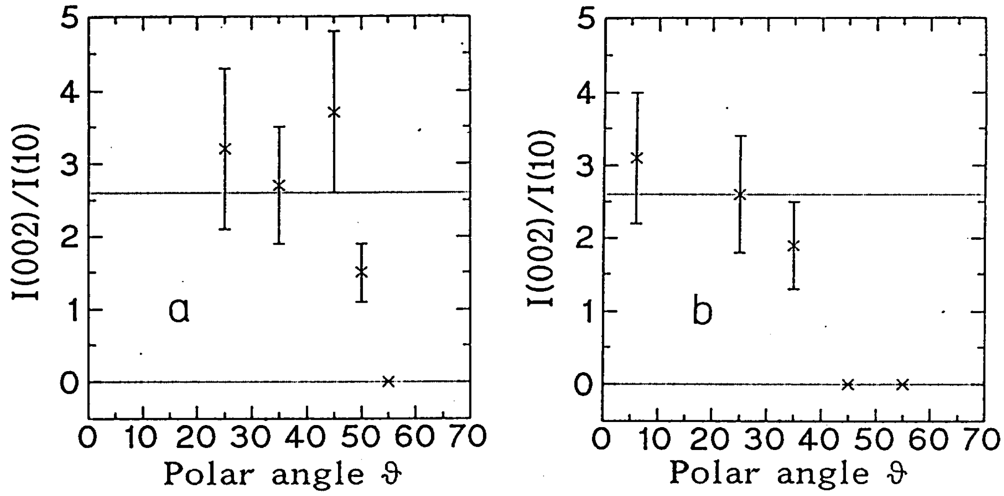

Fig. 6: Crystalline orientation as a function of polar angle ϑ for two power densities
a) 1.6 GW/cm^2 b) 0.7 GW/cm^2

Density and resistivity of carbon layers prepared by laser plasma ablation-deposition as a function of laser power density on the carbon source

Carbon layers prepared by laser plasma ablation-deposition are quite different in their physical properties compared to all other types of carbon layers. That is why the density and resistivity of such layers were measured for six different laser power densities used for preparation. The samples used for the density measurements were mounted in a distance of 20 cm from the target at a polar angle $\vartheta = 14°$. The substrate was a polished silicon wafer on which a 50 μm thick nickel mask with an aperture of 4 mm × 1.5 mm was fixed by means of a permanent magnet from the back side. A carbon thickness of 20 μg/cm^2 was deposited, which was controlled by a quartz crystal sensor mounted as close as possible to the aperture at the rim of the wafer. One deposition by thermal evaporation (ec-foil) was done for comparison with the layers prepared by laser plasma ablation. After deposition the mask was released and the height of the rectangle was scanned by the needle of a Tencor α-step. The height was compared to the thickness reading (μg/cm^2) of the quartz crystal sensor in order to calculate the density. The densities in dependence of the laser power density are tabulated in table 2.

Within the error the density of carbon layers prepared in the range of 1.4 to 16 GW/cm^2 do not differ from the density of a graphite single crystal, which is surprising, because the electron diffraction pattern prove a nearly amorphous structure with only carbon crystals of nm size. This is an indication that some carbon is compacted by sp^3-bond. This portion is increasing with laser power density, especially at 230 GW/cm^2 the density is clearly above the one of a graphite single crystal. The density of a carbon layer prepared by thermal evaporation- condensation (ec-foil) is within the error in agreement with the density of 2.01 ± 0.03 reported by Stoner.

In order to measure the resistivity of the carbon layers glas substrates were mounted at nearly the same geometry as the silicon wafers for the density tests. Both substrates were carbon coated in the same deposition process. On the 3.2 mm wide glass substrates gold contacts with a distance of 3 mm were deposited by vacuum evaporation condensation. With a voltage of 50 mV the resistance of the 3.2 mm × 3 mm carbon layer was measured. With the density and thickness data from the same deposition process the resistivity could be calculated and is plotted in table 2. The data show no correlation to the laser power density. Especially the layer deposited at 230 GW/cm^2 shows the lowest resistivity which is in contradiction to the density data which favour some amount of sp^3-bonds. The resistivity, however, should increase with the amount of sp^3-bonds. Only in comparison with the ec-layers the resistivity is higher by four decimal powers.

power density [GW/cm^2]	density [g/cm^3]	specific resistance [Ωcm]	
1.4	2.15 ± 0.03	—	
1.6	2.44 ± 0.24	124 ± 15	
2.4	2.22 ± 0.22	192 ± 23	
8.0	2.03 ± 0.20	260 ± 31	
16.0	2.45 ± 0.25	245 ± 30	
230.0	2.80 ± 0.28	103 ± 12	
ec-foil	1.94 ± 0.19	0.015 ± 0.002	
single crystal of	2.26	$\approx 10^{-4}$	perpendicular to c-axis
graphite		≈ 1	parallel to c-axis
fine grain graphite	1.75 - 1.9	$1.5 - 1.8 \cdot 10^{-3}$	
diamond	3.5	$\gg 10^{16}$	

Table 2: Density and resistivity of lpa-layers in comparison with other forms of carbon

First tests with the new Nd:YAG continuous wave laser

The 14 years old Nd:YAG laser (2660-1R Holobeam) had several break downs. Once even the laser rod broke without detectable reasons and had to be replaced. Finally it was noticed that there were thermal problems, which had deformed the plastic housing of the laser cavity. The laser company was not able to find spare parts. An exchange of the laser head by a new one seemed to be not economical because also the power supply had had several break downs, and it was not clear how long there would be possibilities to repair it. That is why it was decided to buy a new laser. It is the SL 904 Nd:YAG continuous wave laser from Spectron Laser. The maximum laser power of about 110 W comes from a 130 mm long and 5 mm in diameter laser rod. The divergence of the laser beam is about 10 mrad. With the existing upcollimator of 6 : 1 the expanded laser beam has a diameter of 30 mm and offers the same adaptation to the vacuum system as the old laser.

First tests with the new laser were done with material amounts of $\approx$ 1.5 mg of LiF and U_3O_8. Both materials in powder form and just centered in the crucible by means of a small spatula, because these small amounts could not be pelletized. In order to avoid scattering of the powder grains, it is undispensable to start the heating of the fluoride or oxide with zero laser power. This is one advantage of the new laser, that the laser power gradient has no offset.

Total evaporation was achieved after a 15 minutes exposure to a focused 30 W laser beam, continuously scanned on all the grains placed in the crucible. After each uranium oxide run a thin black layer was left in the crucible, this material could not be evaporated, even when the laser power was raised to 110 W. This was due to some calcined residues of organic impurities, present in the uranium oxide.

Segmented ferromagnetic Fe layers for transient magnetic fields experiments
(in cooperation with K.-H. Speidel)

Transient magnetic fields experience perturbations when beams of heavier ion are applied. It has been suggested that the perturbations might propagate very quickly over a large distance in the ferromagnetic layer due to the characteristic domain structure of the ferromagnetic matter. In order to eliminate this propagation, targets with an iron layer consisting of separated segments were required.

Iron layers consisting of the separated segments were prepared by evaporation-condensation in high vacuum through suitable mesh masks. These were circular nickel masks of 4 μm thickness and 3.05 mm in diameter with meshes of 50 μm width of tetragonal or hexagonal shapes, used normally as frames for electron transmission microscopy. 3 mg/cm^2 Fe layers consisting of the separated segments were prepared on Al foil backings heated to $\approx$ 600 K during the iron deposition.

The magnetic properties of the segmented Fe layers were insufficient for both types of mesh masks used during deposition. Neither the tetragonal nor the hexagonal mesh masks resulted in layers with satisfying magnetic properties. The first measurements were done with the induction coil magnetometer. As its signal depends on the mass of the specimen it was considered that these segmented samples could be too small for this kind of test. That is why the magnetic properties of the segmented Fe layers were checked with a Faraday balance, which requires optically plane layers. In order to eleminate possible attenuation caused by insufficient plane Al backings, the segmented Fe layers were additionally prepared on highly polished silicon substrates. The Faraday balance showed no magnetic saturation even in an external magnetic field of $\geq$ 0.1 T.

There seems to be no major differences comparing the use of these two backing materials, because Fe films prepared in the same evaporation charge but without mesh masks showed the well known good magnetic properties for Fe layers on both backing materials. These results were indipendent from the type of measurement, magnetometer or Faraday balance.

4.2.3 Operation of the Q3D magnetic spectrograph

T. Faestermann

The Q3D spectrograph was again extensively used for a large variety of experiments. In 1992 it was operated for 110 days, corresponding to 38 % of the beam time for experiments.

One major problem occurred in september, when a water leak developed in one coil of the main quadrupole. A winding on the surface of the coil was corroded on a length of about 15 mm and about half the cross section of the 5x5 mm^2 copper tube had been destroyed. Apparently there had been insufficient insulation against the opposite coil and a leakage current lead to the corrosion. With the help of the workshop a copper piece was fitted into this opening and soft soldered in such a way, that the cooling water could pass the tube without an increased resistance but did not leak out of the tube. Ten days after the occurence of the dammage, the spectrograph was operational again. The coil carries the full current and has shown no further problems. Nevertheless a new set of quadrupole coils will be ordered.

After the removal of the PDP10 computer, we had to change the loading procedure for the Z80 microprocessor, which controls entrance slits, target position and angle and the rotation of the spectrograph and the top of the target chamber. The microprocessor is now loaded from a central Atari computer, which serves also as its terminal. These programs can be called from the main program "Q3D", which calculates the kinematics for a given reaction and sets the values for the calculated magnetic fields in the dipole magnets and the main quadrupole.

In the high resolution ERD experiments, the higher components of the multipole element, namely hexapole and octupole, have been used for the first time to correct for the large kinematic shifts. For the octupole the current available from the existent power supply was not sufficient and it turned out that the power supply did not work reliably. Therefore this power supply has been replaced. The appropriate current values will also be set automatically.

4.2.4 Adaption of the cathode strip focal plane detector for the Q3D spectrograph to the MLLE/CADMUS data aquisition system and development of a new single strip readout electronics

J.Ott, H. Angerer, W. Schauer, T. von Egidy

Adaption to the new data aquisition system

The light ion detector with single cathode strip readout is used for investigations of transfer reactions. It is placed in the focal plane of the Q3D magnetic spectrograph and consists of 3 branches (Fig. 1).

The first is a scintillator giving the energy rest signal caused by stopping the charged particles. Both other branches together work as a multiwire proportional chamber. Two anode wires give an energy loss signal, while the position information is derived from the charge influenced on a few of the 114 cathode strips (Fig. 2), each equipped with its own preamplifier (mounted in the detector box), pulse shaper and ADC [1, 2]. Correct events are selected by an ASIC [4]. It determines the multiplicity and the start address of the event. The multiplicity is the number of cathode strips on which sufficient charge is influenced. A survey of the datastreams from the detector to the display of spectra is given in Fig. 3.

We operate the detector in the way described in [3] and [5]. For each valid event two T800 transputers perform a gaussian fit to the charge distribution influenced on the cathode strips (Fig. 2). With this method the systematical error can be reduced [5].

To read out the position information of the transputer it was necessary to adopt the hardware handshake signals in the way needed by a SMDW (**S**ingle **M**ulti **D**igital **W**indow, a special input module for digital signals) as the suitable CAMAC interface.

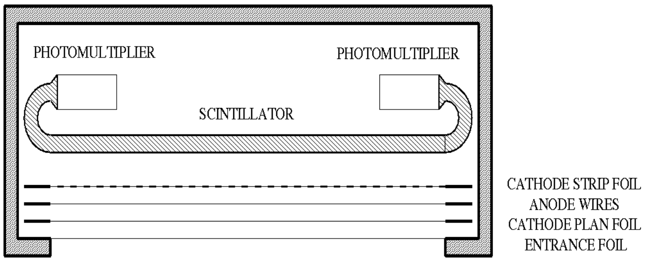

Fig. 1: Scheme of the detector

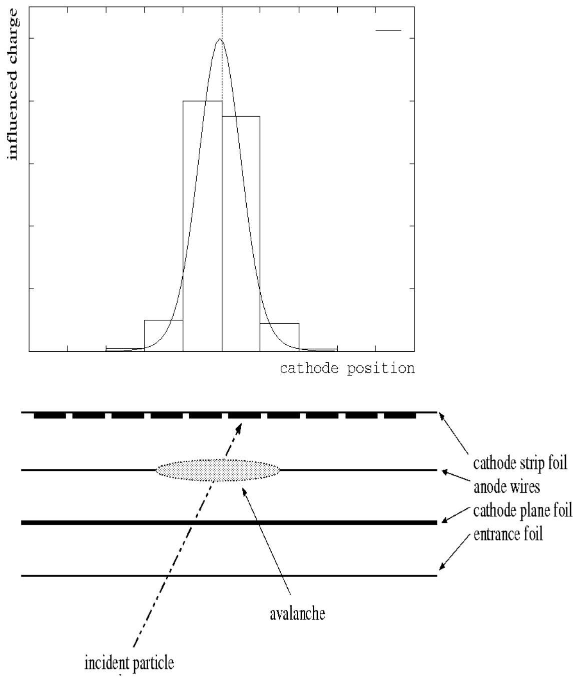

Fig. 2: Scheme of the charge distribution of the cathode strips.

Consequently, a new coincidence circuit and a new generation of master trigger had to be built with NIM modules. On the software side new parameter files and tasks had to be written. All this was sucessfully done and in autumn the first spectra could be measured.

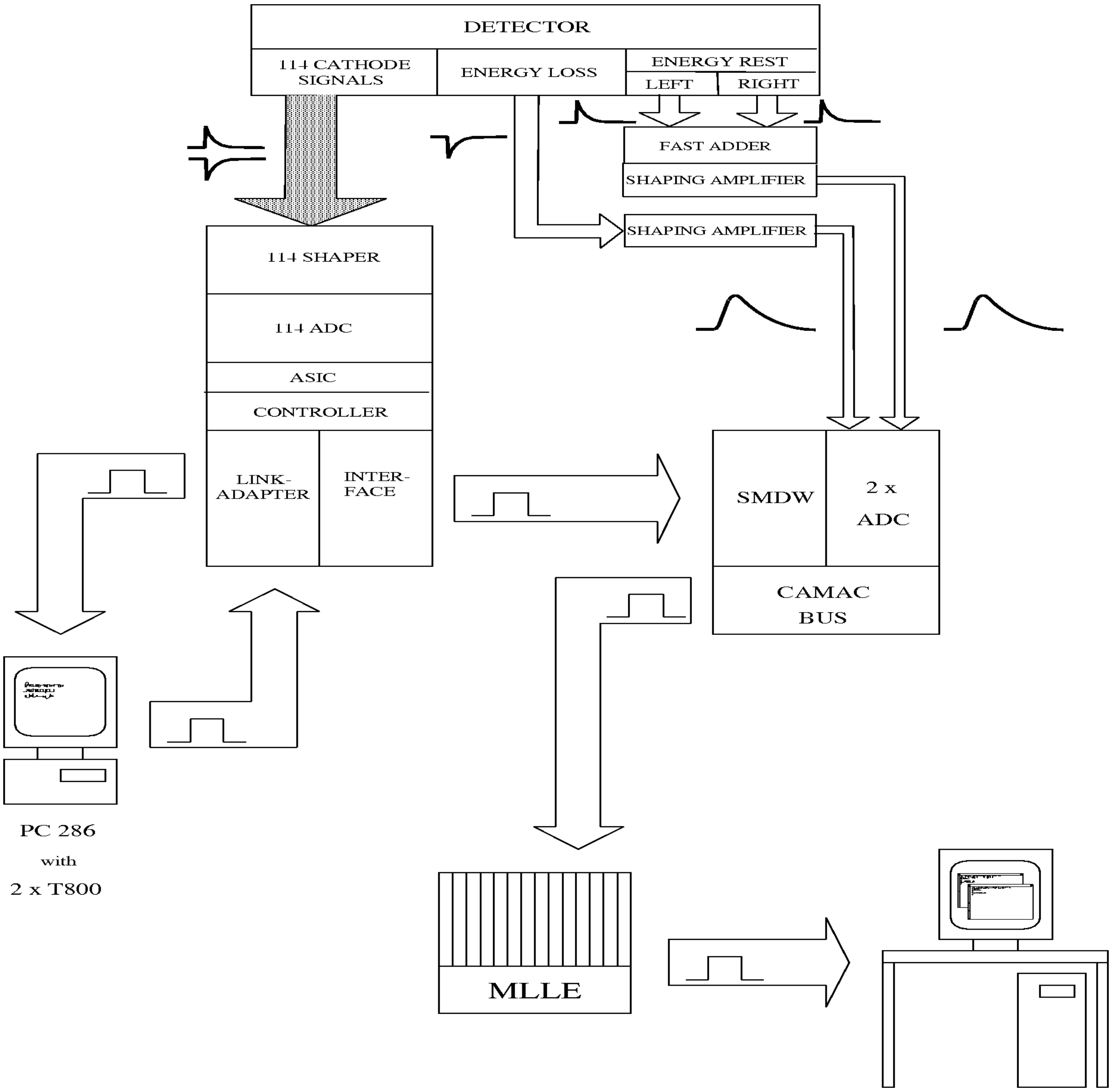

Fig. 3: Survey of the datastreams, without coincidence circuits.

A new concept for readout electronics

When operating the detector with the transputer method we recognized that there are some disadvantages caused by the fact that all developments up to now were limited by the PDP15/10 system. Data can be transferred into a SMDW after a transputer fitting time of about 570 μs. Together with the CAMAC readout time for the SMDW and the ORTEC 413A ADC (energy loss and energy rest signals) this leads to a total dead time of about 700 μs which limits the rate of data aquisition to 1.4×10^3 counts per second. We confirmed this when we tested the experimental setup with a pulse generator. Furthermore all information about the original values of the ADC's and the fit parameters are lost.

With the new powerful computing and data aquisition structure both the aquisition rate can be increased and more fit parameters can be analysed. The new concept bases on the fact that all valid events passing the ASIC described in [3] and [4] have a multiplicity between 3 and 7. That means that 8 parallel working ADC's are sufficient when multiplexing the analog signals to it.

The cathode strips, preamplifiers and pulse shapers are used like before. For each strip the signal passes from the shaper into a discriminator and a peak hold unit (Fig. 4). If the lower discrimination level is exceeded, a logical signal is sent to the ASIC while the maximum of peak is detected and stored in the peak hold part. Using the 'active' signals from all strips the ASIC determines whether an event has valid multiplicity. If it is valid, the start address is calculated and sent together with the value of the multiplicity to the multiplexing controller. Otherwise all components are resetted [4]. The ASIC finishes its work in about 1.5 μs. Since the time constant of the pulse shapers is 2 μs, there is no waste of time caused by the ASIC.

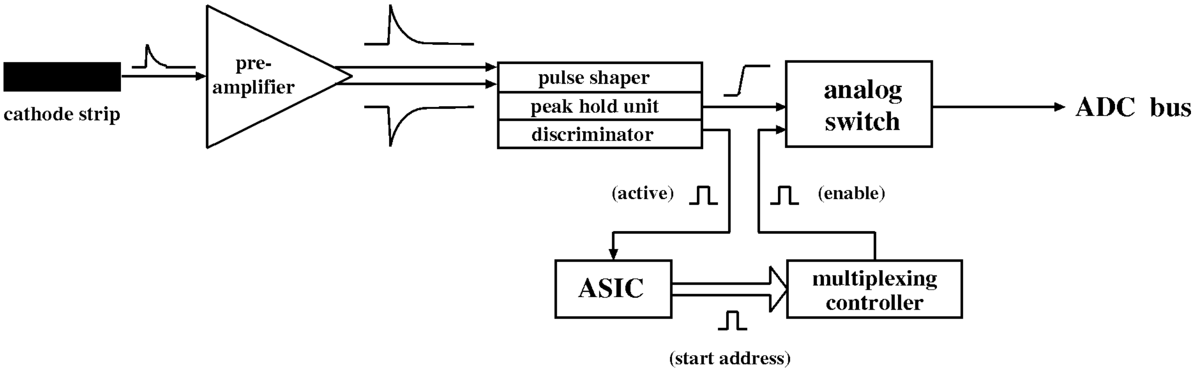

Fig. 4: Scheme of new readout for each single strip.

The analog switch of the strip related to the start address and the switches related to the next 7 addresses are enabled by the controller to transfer the analog signals via a bus to the ADC's (Fig. 5). These are of the 10 bit hybrid type with a conversion time of 0.65 μs. A parallel transfer of the ADC data via a twisted pair line would need 160 wires from inside the Q3D hall to the CAMAC crate in the computer room. Furthermore a few handshake and controll signals are necessary, e.g. to check coincidence. Therefore, we decided to achieve the transfer by multiplexing in 4 blocks of 2 ADC outputs which needs only 40 wires. These 40 digital signals are connected to 2 digital input registers in a CAMAC crate.

The coincidence test of the position, the energy loss and energy rest signals is performed during the shaping and conversion time. In the case of a positive result, first the start address and the multiplicity from the ASIC and then the ADC values are multiplexed to the input registers (block 1 in Fig. 5). The latter multiplexing starts with the block 'i', 'k', 'l' or 'm', which contains the value of the start strip. Then the other blocks are cyclicly read out. In cases of even start addresses the first ADC, which is read out, is related to the strip before the start address and therefore has always the value zero. This is caused by the kind of multiplexing and can be taken into account by adding one 'if - then' condition to the task in which the spectra are created.

The digital input registers are read out 5 times and during the same time the ORTEC 413A ADC converts both energy signals and is read out afterwards. To see immediately during the running experiment whether all components work properly, the position of the event is calculated in the MLLE 68030 processors by the center of gravity method as used in [1]. Here the systematical error of the position calculation does not play a role. When operating in this way the data aquisition rate should increase by a factor two.

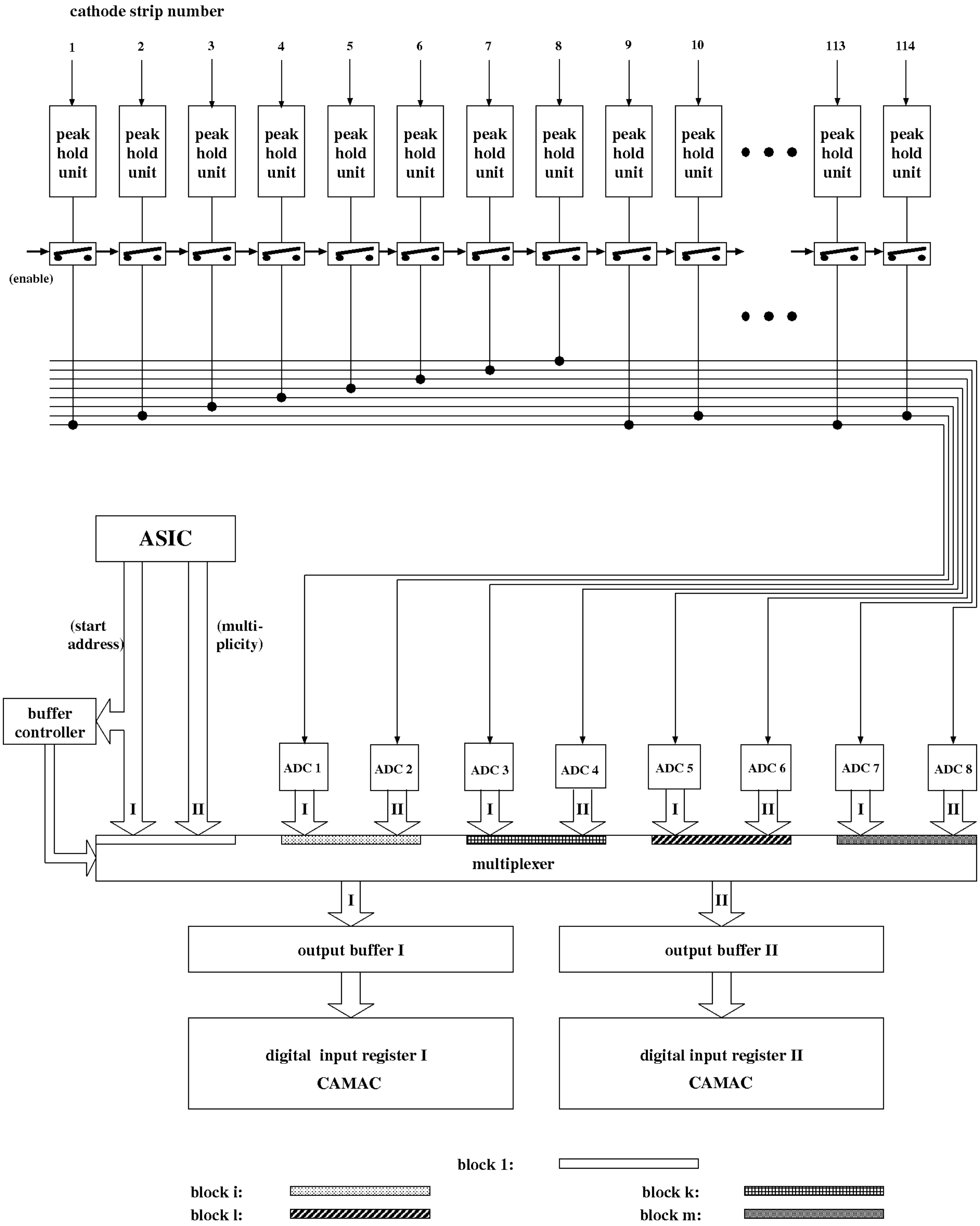

Fig. 5: Scheme of multiplexing the analog signals to the ADC's and input registers.

Later in an off-line run there is enough time for a more detailed analysis. That means that all advantages caused by saving the original ADC values can be used. The fit of the charge distribution of the cathode strips has to be performed only for events corresponding to the given filter conditions. As this is reducing the calculation time by a factor of about 50, one can use a better fit function. We propose a superposition function consisting of 75% gaussian and 25% hyperbolic secant [5]. Also a more exact fit procedure can be used. Investigations about this have shown that all events of interest for a typical spectrum can be fitted in about 12 seconds CPU time when using a Marquardt procedure on one of the faster UNIX machines [6].

A further advantage of this method is that the ADC values give hints for optimizing the signal stretching of the shapers. For geometrical reasons (Fig. 2) there is a relation between the calculated FWHM of the charge distribution of the cathode strips and the angle of incidence of the detected particles. Setting additional filter conditions to it, may moreover improve the resolution of the detector.

Up to now single prototypes of the peak hold and ADC circuits are sucessfully tested. Next steps are developing the multiplexing controller and combining all the hardware. In parallel the necessary new software for the data aquisition has to be written. Then first tests using these prototypes for reading out 16 cathode strips will be performed.

Supported in part by DFG.

[1] H.Lindner, H. Angerer and G. Hlawatsch, Nucl. Instr. and Meth. **A 273** (1988) 444
[2] H. Lindner, PhD thesis, 1989
[3] H. Lindner et al., Jahresbericht 1989, p. 162
[4] H. Hiller, diploma thesis, 1989
[5] H. Trieb, diploma thesis, 1990
[6] W. Schauer, diploma thesis, 1993

4.2.5 A silicon detector array for ultra high vacuum applications

J. Friese, F. Heine, E. Kellner, H.-J. Körner, M. Peter

Ultra high vacuum conditions (p $< 10^{-6}$Pa) have become increasingly important in numerous fields of physical research. Experiments in nuclear and atomic physics require storage rings like the ESR (GSI, Darmstadt) or the cooler ring at IUCF (Indiana, USA) as modern tools in basic research. These storage rings have to be operated at minimum residual gas pressure in order to maintain the required beam quality for reasonable timescales ($\tau = 1$ d). In other applications, e.g. material analysis with nuclear physics techniques, it is important to avoid the contamination of clean surfaces by adsorbation of residual gas particles. In both cases it is often necessary to detect low-energy ions ($\leq$ 1MeV/A) with good energy and/or spatial resolution.

We have started to investigate the nuclear structure of unstable nuclei by means of direct reaction mechanisms [1]. Further (p,p′) [2] – and (d,p) [3]–reactions with radioactive projectiles (i.e. ^{56}Ni and resp. ^{55}Co, ^{46}K, ^{134}Te) will be performed in near future at the ESR. In these reactions the recoiling protons of interest emerge from the target at laboratory angles around $\Theta_{Lab} \leq 90°$ with kinetic energies 100 keV $<$ E$_{kin}$ $<$ 10 MeV. To achieve the required excitation energy resolution for the reactions to be investigated, the strong kinematic variation of E$_{kin}$ (Fig. 1) has to be matched by both, a good spatial and energy resolution of the detectors. Therefore no additional window foil (energy loss, multiple scattering) is allowed to separate the detector from the ultra high vacuum at the ESR. Furtheron, due to the limited luminosities $L \sim 10^{27} s^{-1} cm^{-2}$ expected, the proton detectors have to cover a large fraction of the accessible solid angle.

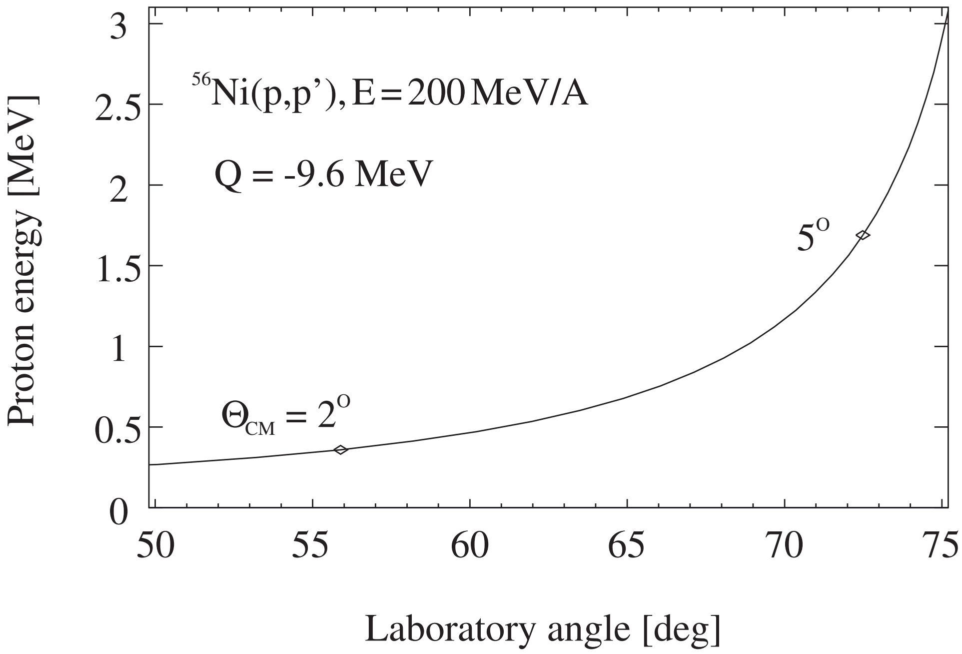

Fig. 1: Expected angular range for inelastic scattered protons after excitation of the M1 resonance in ^{56}Ni at $E^* = 9.6$ MeV [2]

In the Munich Tandem laboratory several groups work on high precision material analysis involving heavy ion beam scattering and sputtering techniques [4, 5, 6, 7, 8]. For quantitative measurements well defined surface conditions, and therefore a UHV environment, are mandatory. A monitoring analysis of the sputter target by means of elastic recoil detection analysis (ERDA) [5] would be very desirable [9]. As the low energetic recoils ($E \leq 1$MeV/A) would be absorbed in any window foil, the detector has to be mounted directly in the UHV chamber.

For applications in the ultra high vacuum two major requirements have to be fulfilled:

- The detector has to resist a baking procedure without changing its performance.
- A pollution of the vacuum has to be avoided.

Silicon detectors seem to be the optimum choice to match all the above constraints. However, commonly used housings, supports and electrical contacting techniques cannot be used. We have therefore built a prototype silicon detector array ($A = 16cm^2$) of 4×4 PIN–diodes ($a = 1cm^2$, SIEMENS F171A). The array has been assembled on a ceramic support consisting of two frames pressed together (Fig. 2). As a workable ceramics we have chosen MACOR which allows precise substructures of less than 500μm extension, a necessity given by the average thickness of the silicon chips.

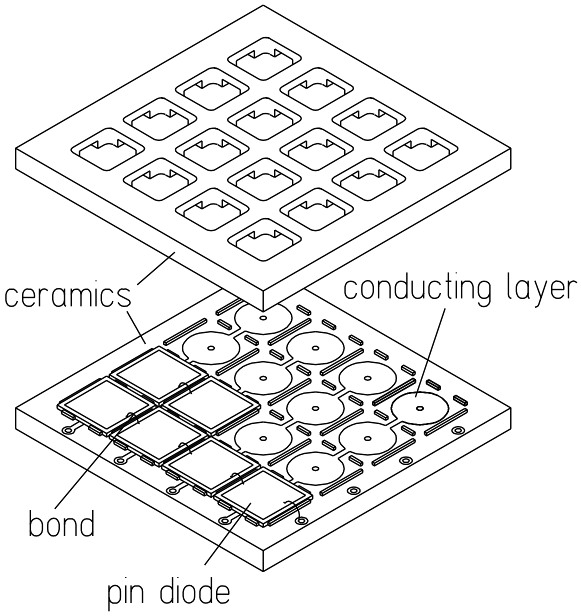

Fig. 2: View of a PIN diode array usable in the UHV.

To cover the ceramics with a conductive layer suited also as bonding pads, a particular sputtering technique had to be developped. A $d = 20\mu m$ thick gold layer was placed on a platinum backing ($d = 5\mu m$), sputtered onto the MACOR surface. The assembled detector does not contain any outgasing hydrocarbons.

The device was baked for 24 hours at $T = 200°C$ in the UHV chamber, installed at the Tandem experimental hall by W.Assmann and his group [8]. A pressure of $1.5 \cdot 10^{-7}$Pa was reached using only a turbomolecular pump. With the help of a titanium sublimation pump the pressure decreased after another 24 hours to $4.3 \cdot 10^{-9}$Pa. The mass spectrum of the residual gas shown in fig. 3 reveals no unusual and severe pollution of the vacuum.

The detector performance was tested with α–particles from a mixed nuclide source before and after baking. For the readout of the signals the front contacts of the diodes are connected in columns, the rear contacts in rows. All electric contacts survived, no hints for increased leakage current and noise contributions to the detector signal were found. The energy of the particles is measured in separate electronic chains for rows and columns. A representative α–spectrum for one diode, gained with the help of this matrix readout technique [10], is presented in fig. 4 showing a satisfying energy resolution of $\Delta E = 21$ keV (fwhm).

Further developments will concern the implementation of μ–strip detectors, single diode read out, bakeable signal cables, and vacuum feedthroughs.

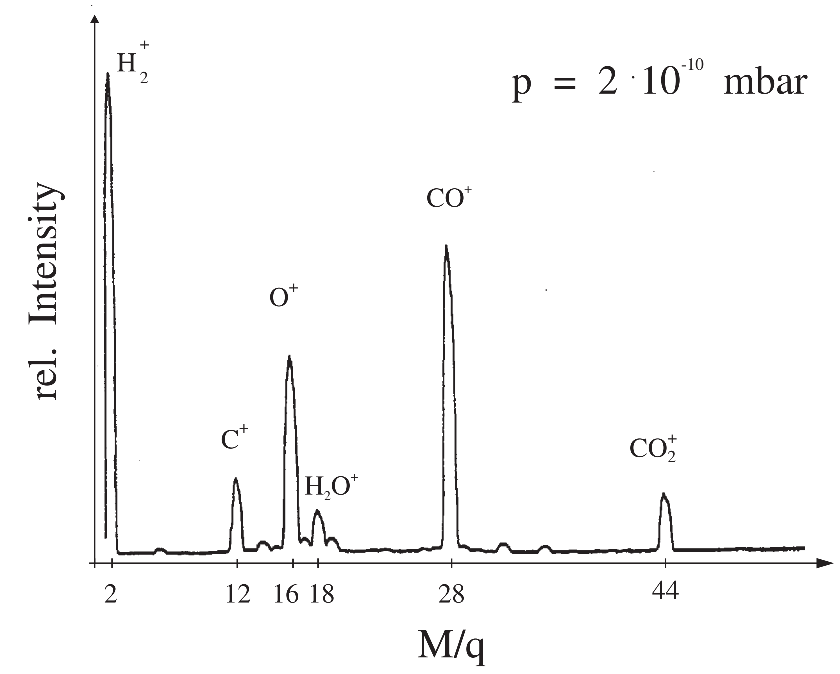

Fig. 3: Mass spectrum of the residual gas at a pressure of $2 \cdot 10^{-8}$ Pa ($= 2 \cdot 10^{-10}$ mbar).

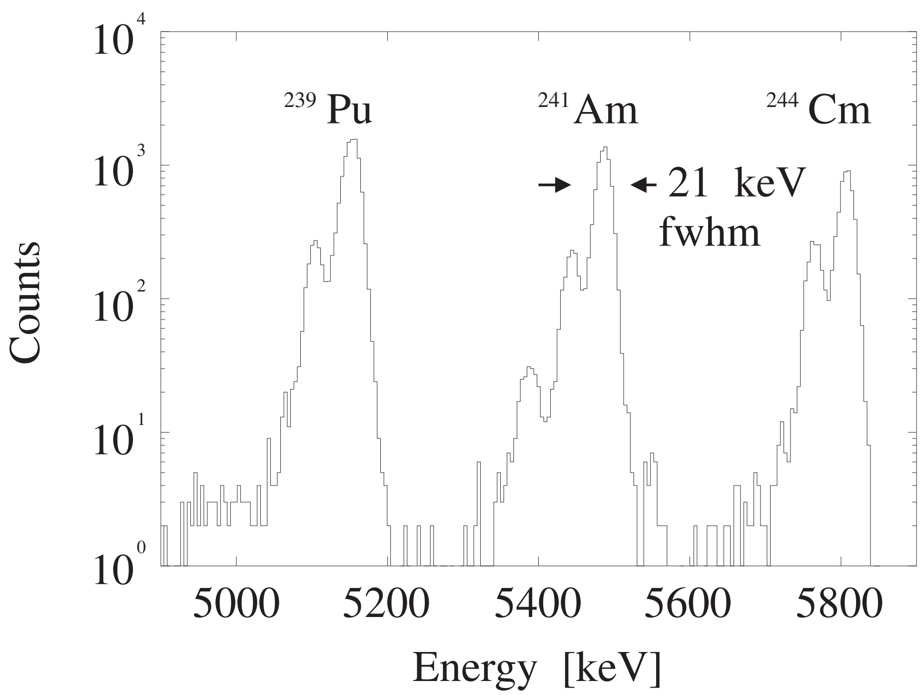

Fig. 4: Energy spectrum of α–particles, recorded after 24 hours of baking.

[1] J. Friese et al., this report
[2] J. Friese et al., ESR–proposal no.E022
[3] P. Egelhof et al., ESR–proposal no.E023
[4] W. Assmann et al., Jahresbericht 1990, p.107
[5] G. Dollinger and W.Assmann, Jahresbericht 1990, p.110
[6] W. Assmann et al., Jahresbericht 1991, p.92
[7] G. Dollinger et al., Jahresbericht 1991, p.97
[8] W. Assmann et al., this report
[9] W. Assmann, private communication
[10] J. Friese et al., GSI–Report 90–1, p.297

4.2.6 The "Charge State Enforcer" revisited

K.E.G. Löbner

The possibility to use a charge state enforcer to accelerate radioactive ion beams with high acceleration efficiency has been investigated.

The idea of the charge state enforcer has been published by J.G. Cramer [1] and later by Franzke et al. [2] and V.P. Kukhtin et al. [3]. The general idea of this method is to select behind a stripper foil all ions of one charge state and force the ions with other charge states to circulate back to the stripper foil repeating the stripping and subsequent selection process again and again until "nearly all" ions have the wanted charge state and are sent to the next acceleration step.

According to a recent publication by Shima et al. [4] only 20 % of the ions are in the most abundant charge state for heavier nuclei ($Z \geq 40$) with E/u = 0.01 to 3 MeV/u. That means one looses $\approx$ 80 % of the original heavy ion intensity with one stripping process and $\approx$ 96 % with two stripping processes. That is the reason why it is worthwhile to think about methods to decrease these losses, e.g. with the charge state enforcer.

The investigation has yielded the following results: In addition to the technical realization problems for the selection of ions with one charge state (which is certainly not simple and cheap) the charge state enforcer yields a considerable degradation of the beam quality due to energy losses and small angle scattering for many passes of the stripper foil or gas. The energy loss of the ions should be compensated by accelerating the recirculating ions after each pass of the stripper. To achieve this for all ions, the ions with different charge states should pass the high frequency acceleration gap at certain phase points of the high frequency, as suggested already by Franzke et al. [2]. Especially at low energies ($\approx$ 0.1 MeV/u) the small angle scattering is expected to yield problems. With a thin gas stripper the realization of a recirculating stripper system may be possible in principle. To use this method the pulsed beam structure before and behind the charge state enforcer must be matched. It is certainly necessary to investigate the whole acceleration process and how the transmission is influenced by the degradation of the beam quality and the pulsed structure of the beam.

[1] J.G. Cramer, Nucl. Instr. and Meth. **130** (1975) 121
[2] B. Franzke, K. Blasche, B. Franczak, GSI-J-1-78, p. 157
[3] V.P. Kukhtin, Yu.P. Savergin, I.A. Shukeilo, Particle Accelerator Conference 1991, San Francisco, IEEE 91 CH 3038-7, p. 2035
[4] K. Shima, N. Kuno, M. Yamanouchi, H. Tawara, Atomic Data and Nuclear Data Tables **51** (1992) 173

4.2.7 Developments for mass measurements of exotic nuclei at the ESR

K. Balog, T. Beha, Th. Kerscher, K.E.G. Löbner, Th. Winkelmann, Ch. Klein [a], A. Magel [a], T. Radon [a], D. Rosenauer [a], H. Schäfer [a], E. Schneider [a], D. Scholten [a], M. Sendor [a], J. Trötscher [a], B. Vogel [a], H. Wollnik [a], H. Eickhoff [b], H. Geissel [b], G. Münzenberg [b], B. Franczak [b], B. Franzke [b], Y. Fujita [c], and D.J. Vieira [d]

[a] 2. Physikalisches Institut der Universität Giessen

[b] Ges. für Schwerionenforschung mbH, Darmstadt

[c] College of General Education Osaka University, Japan

[d] Los Alamos National Laboratory, Los Alamos

A Time-Recording-System (TRS) for the mass measurements of exotic nuclei at the Experimental-Storage-Ring (ESR) at GSI, Darmstadt is under construction in Munich. The hardware development of the TRS will be completed in the next weeks. A first software version of the TRS-program is running. Detailed information about the operating principle of the TRS and its electronics were presented in the last two annual reports [1].

Last year, the main hardware problems were level adaptations and temperature shifts in the fast ECL-logic circuits, the selection between the four circuits of the TRS and broken connections on the printed boards. After installing additional ventilators and adjustable level-shifters for the fine- and coarse time circuit, the ECL-parts of the electronic are working. The correct selection between the four circuits was achieved by redesigning parts of the control unit. We produce now the reset-signal for the ECL-buffers with a fixed timing to the write-signal of the Flash ADCs. The TRS is working in principle, but a fine adjustment of the timing for the control signals has to be done now.

The TRS can be calibrated by sampling its 50 MHz sine-wave with a sampling time of 200.077 ns. The difference between the sampled and the ideal sine-wave is composed of a systematic error (which will be corrected for with software) and the jitter of the sampling unit. We have seen in first calibration cycles, that the jitter of the sampling unit is less than 40 ps. Therefore, we think, that the time-resolution design aim (< 35 ps) should be reachable with the TRS.

A stepper-motor control for the vacuum lock system, that will enable the detector to be installed or removed from the ESR without breaking the vacuum in the ring, has been adapted and completed. It is planned, that all the ESR-, vacuum- and high voltage settings should be connected with the TRS data and stored on tape.Therefore a data acquisition system should be running on a VAX. The part of the acquisition system, which will collect the TRS data from our PC via ethernet, is running. However, at the moment it is too slow for the expected data rates of the planned experiment at the ESR.

The timing detector system, which was developed by the Giessen group, has been tested with $^{18}O^{8+}$-ions of 700 MeV/u at the final focus of the Fragment-Seperator (FRS) at GSI [2]. The timing properties were measured in coincidence with a second set of mircochannel plates. A detection efficiency of about 60 % and a timing accuracy of about 150 ps (FWHM) has been achieved.

The fine adjustment of the TRS and final tests will be done in the next weeks. We started also with the construction of a second improved TRS, considering all our experiences with the first one. The software must also be improved. For instance, the transputer programs must be distributed over more transputers. The VAX-PC- connection should be completed as soon as possible.

[1] K. Balog et.al., Jahresbericht 1990, 207
K. Balog et.al., Jahresbericht 1991, 174

[2] J. Trötscher et.al., **GSI93-1**, to be published